Spatially tunable noncritical phase matching of second-harmonic generation in a doped LiNbO$_3$ crystal

Georgiy Shoulga, Gilad Robert Barir, and Alon Bahabad
Department of Physical Electronics, School of Electrical Engineering, Fleischman Faculty of Engineering,
Tel Aviv University, Tel Aviv 69978, Israel

We present, theoretically and experimentally, phase-matched noncritical off-axis second-harmonic generation which is easily tuned using a spatial light modulator. The phase-matching condition depends on both the spatial properties of the fundamental beam and the thermal properties of the medium. We show that a thermally induced phase mismatch can be compensated by choosing the pump beam spatial properties resulting in phase-matched noncollinear second-harmonic generation.

I. INTRODUCTION

Phase matching (PM) in crystals is usually achieved either by critical PM, where the angle orientation of a birefringent crystal is the matching parameter, or by noncritical PM (NCPM) (also called temperature PM), where the temperature T of the crystal is the matching parameter. Critical PM and NCPM have been widely studied and experimentally demonstrated in various nonlinear bulk crystals and optical waveguides [1,2]. Noncritical PM can also be achieved when ordered modulation of the properties of the medium is used to satisfy momentum conservation of the photons involved in the process, in what is known as quasi-phase-matching [3].

In second-harmonic generation (SHG) two photons of the fundamental beam are combined to produce a second-harmonic (SH) photon at a doubled frequency. We denote the fundamental (pump) field by subscript p and the SH (signal) field by subscript s. The pump of wavelength λ_0 propagating in the crystal is influenced by a temperature-dependent refractive index $n_p \triangleq n(\lambda_0, T)$. Analogously, the SH is subject to a refractive index $n_s \triangleq n(\lambda_0/2, T)$.

Lithium niobate is a useful nonlinear material for its uniquely large second-order nonlinearity. Lithium niobate crystals used for noncritical PM are usually doped due to a strong photorefractive effect, which damages the crystal at high temperatures. The dopant is often MgO, as in the crystal we use here (5% doping [4]), having a critical temperature of about $114.5\,^\circ$C [5].

Spatial light modulators (SLMs) are widely used to control the phase front of an optical beam. Spatial light modulator-based pump field shaping has been used to obtain SH of desired shapes [6] or to achieve PM [7], both through a machine-learning algorithm. Spatial light modulator-based field shaping was also used to achieve tunable on-the-fly all-optical quasi-phase-matching of high-harmonic generation in gases using a pump composed of a superposition of Bessel and Gauss beams [8]. Here we utilize SLM-based beam shaping to tune the spatial properties of the pump beam in SHG to allow phase matching in the presence of temperature-induced phase mismatch.

II. THEORY

Second-harmonic generation in birefringent crystals is often observed in an on-axis collinear scheme [Fig. 1(a)], where the fundamental and signal beams propagate along the same axis. Assuming energy balance $2\omega_p = \omega_s$, a relevant NCPM condition for SHG reads $\Delta k_{cl} \triangleq 2k_p - k_s = 4\pi(n_p - n_s)/\lambda_0 = 0$, where λ_0 is the fundamental wavelength and cl stands for collinear. Therefore, the PM condition is $n_p = n_s$, achievable by tuning the crystal's temperature. We denote the NCPM temperature by T_{pm}^0, i.e., $n_p(T_{pm}^0) = n_s(T_{pm}^0)$. For example, collinear PM can be achieved using a loosely focused Gaussian beam (FGB). We indicate the k-vectors corresponding to an FGB by k_p^G.

A collinear off-axis PM scheme for SHG is shown in Fig. 1(b) and it can be achieved using a focused ring beam (FRB). We add a superscript B to its k-vector denotation k_p^B to indicate it produces a Bessel beam in the vicinity of the focal point. The case in Fig. 1(b) results in a conical shape of the generated SH signal, with the apex at the focal point. Superimposing an FGB and an FRB, a noncollinear PM scheme [Fig. 1(c)] can be observed. Here the generated signal propagation direction is between the directions of k_p^G and k_p^B. Defining $|k_p| \triangleq |k_p^G| \cong |k_p^B|$, the PM condition now reads

$$\Delta k \triangleq 2|k_p|\cos\theta - |k_s| = \frac{4\pi}{\lambda_0}[n_p(T)\cos\theta - n_s(T)] = 0. \tag{1}$$

Obviously, it can be controlled by both the temperature T and the angle θ between the two pump components. This condition describes an off-axis spatially tunable noncritical phase matching (STNPM). For $\theta = 0$ we recover the collinear phase mismatch $\Delta k(\theta = 0) = \Delta k(T) \triangleq \Delta k_{cl}$, which is purely thermally induced.
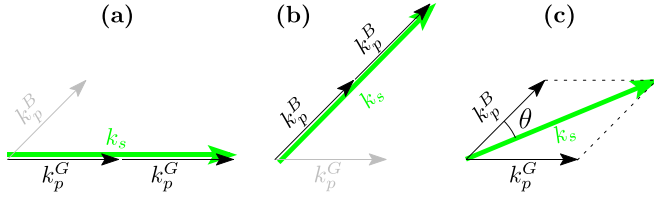
FIG. 1. (a) Collinear on-axis, (b) collinear off-axis, and (c) non-collinear schemes of PM in SHG. The generated SH k-vector is shown in green. Phase mismatch is assumed to be zero. Gray colored k-vectors do not participate in a PM process.

FIG. 2. Schematic of the simulated system.

Considering a geometric optics treatment of an FRB of radius R focused by a lens of focal length f into a nonlinear crystal, the angle θ inside the crystal is given by

$$2\theta = \arcsin\left\{\frac{n_{air}}{n_p}\sin\left[\arctan\left(\frac{R}{f}\right)\right]\right\}, \quad (2)$$

where n_{air} is the refractive index of the medium between the lens and crystal (usually air) and we accounted for Snell's law in the air-to-crystal transition. Combining Eqs. (1) and (2), the PM (optimal) ring radius R_{opt} is

$$R_{opt}(T) = f\tan\left(\arcsin\left\{\frac{n_p}{n_{air}}\sin\left[2\arccos\left(\frac{n_s}{n_p}\right)\right]\right\}\right). \quad (3)$$

A second-order Taylor series and small-angle approximation of Eqs. (1) and (2) yield $R_{opt}(T) \cong (n_p/n_{air})f\sqrt{8(1-n_s/n_p)}$.

For an annular ring not infinitesimally narrow, there is a range of k_p^B-vector directions [4]. Consequently, PM may occur for a ring of radius R that differs from R_{opt}, as long as $R_{opt} \in [R - W, R + W]$, where W is the half-width of the ring. Therefore, a wider ring should lead to PM for a broader range of temperatures.

III. NUMERICAL RESULTS

We now consider numerically the system depicted in Fig. 2. The initial fundamental field is set at the input plane and propagated for a distance ΔL in air to the nonlinear crystal. It is further propagated inside the crystal of length L_{cr}, taking into account diffraction and nonlinear dynamics. The generated SH at the output of the crystal is propagated for ΔL in air to the output plane. The initial fields of FGB, FRB, and a superposition of the two (including a focusing lens phase) are given by

$$E_G(r, 0) = \frac{2}{w}\sqrt{\frac{P_0}{\pi\varepsilon_0 c}}\exp\left[-\left(\frac{r}{w}\right)^2\right]\exp\left(-i\frac{k_{air}r^2}{2f}\right),$$

$$E_B(r, 0) = \sqrt{\frac{P_0}{\pi\varepsilon_0 c S}}\exp\left[-\left(\frac{r-R}{W}\right)^8\right]\exp\left(-i\frac{k_{air}r^2}{2f}\right),$$

$$E_{G+B}(r, 0) = \left(1 + \frac{2\beta Q}{S} + \frac{w^2\beta^2}{4S}\right)^{-1/2}$$

$$\times \left(\frac{w\beta}{2\sqrt{S}}E_G(r) + E_B(r)\right), \quad (4)$$

where w is the initial waist, P_0 is the total field power, $S \triangleq \int_0^\infty re^{-2[(r-R)/W]^8}dr$, $Q \triangleq \int_0^\infty re^{-(r/w)^2}e^{-[(r-R)/W]^8}dr$, and β
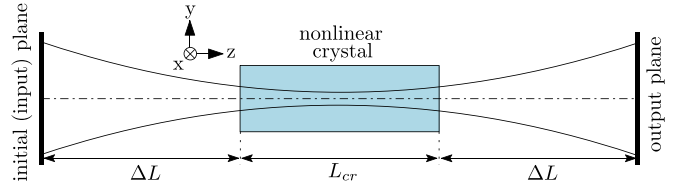
is the ratio of FGB to FRB peak amplitudes. To avoid discontinuities in the ring's profile, we utilize a super-Gaussian envelope of power 8. We consider an ordinary refractive index n_p^o for the pump beam, an extraordinary refractive index n_s^e for the signal [4], a lens of focal length $f = 150$ mm, and a pulse power of 1.175 W.

We perform the simulation in a two-dimensional spatial geometry (x-z plane), utilizing the cylindrical symmetry, to save computation time. Propagation from the input plane to the crystal is performed by standard Fresnel diffraction

$$E(x, \Delta L) = \mathscr{F}^{-1}\left[\exp\left(\frac{-ik_x^2\Delta L}{2k_{air}}\right)\mathscr{F}[E(x, 0)]\right], \quad (5)$$

where $\mathscr{F}[\cdots]$, $\mathscr{F}^{-1}[\cdots]$, $k_{air} = 2\pi n_{air}/\lambda_0$, and k_x are the Fourier transform, its inverse, the wave number in air, and spatial frequency, respectively. The value of ΔL such that the focus would be in the middle of the crystal is a function of f, n_{air}, and n_p^o [4]. Reflection losses in the air-to-crystal transition are neglected. Inside the crystal the pump field A_p is propagated while accounting for nonlinear coupling to the SH field A_s, according to [3,9]

$$\frac{\partial A_p}{\partial z} = \frac{i}{2k_p c^+ c^-}\nabla_T^2 A_p + \frac{2id_{\text{eff}}\omega_p^2}{c^2 k_p c^+ c^-}A_p^* A_s e^{-i\Delta\vec{k}\cdot\vec{r}}$$

$$+ \frac{i}{2}\frac{(s^-)^2}{c^+ c^-}k_p A_p,$$

$$\frac{\partial A_s}{\partial z} = \frac{i}{2k_s c^+}\nabla_T^2 A_s + \frac{i\omega_s^2 d_{\text{eff}}}{c^2 k_s c^+}A_p^2 e^{i\Delta\vec{k}\cdot\vec{r}}, \quad (6)$$

where $k_p = \frac{2\pi n_p^o}{\lambda_0}$ and $k_s = \frac{2\pi n_s^e}{\lambda_0}$ are wave numbers of the pump and SH fields, respectively, and $\Delta\vec{k}\cdot\vec{r} = (2k_p c^- - k_s)(c^+ z + s^+ x)$, with $c^\pm \triangleq \cos(\frac{\theta_2 \pm \theta_1}{2})$ and $s^\pm \triangleq \sin(\frac{\theta_2 \pm \theta_1}{2})$. The two photons that participate in SHG propagate at angles θ_1 and θ_2 in the vicinity of the focal point. Consequently, the PM schemes in Fig. 1 correspond to $\theta_1 = \theta_2 = 0$ (collinear on-axis PM), $\theta_1 = \theta_2 = 2\theta$ (collinear off-axis PM), and $\theta_1 = 0$ and $\theta_2 = 2\theta$ (noncollinear off-axis PM). The effective nonlinear coupling coefficient is $d_{\text{eff}} = 4.4$ pm/V. Pump and SH frequencies are $\omega_p = \frac{2\pi c}{\lambda_0}$ and $\omega_s = \frac{2\pi c}{\lambda_0/2}$, respectively, where c is the speed of light in vacuum. The Laplacian operator ∇_T^2 acts on the fields' transverse coordinate x. The first and second terms on the right-hand side of Eq. (6) represent diffraction and nonlinear coupling of the pump and SH fields, respectively. The third term in the $\frac{\partial A_p}{\partial z}$ equation accounts for noncollinearity. We neglect a signal beam walk-off term $-\tan(\frac{\theta_2 + \theta_1}{2})\frac{\partial A_s}{\partial x}$ as for the maximal θ we used here the maximum walk-off angle θ_{max} is only about 2 mrad. Absorption losses are neglected as well as they were calculated to be 1.5% and 0.3% for the SH
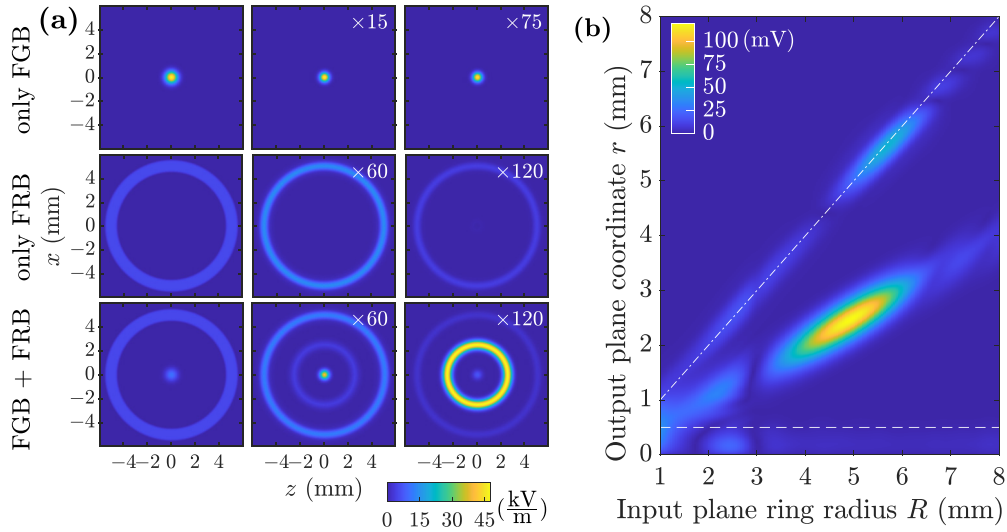
FIG. 3. (a) Field distributions $|E|$ at the input plane (left column) for a FGB (top), a FRB with $R = 4.9$ mm (middle), and their superposition (bottom). Also shown are the corresponding SH distributions at the output plane without (middle column, $T = T_{pm}^0$) and with (right column, $T \neq T_{pm}^0$) thermally induced phase mismatch. Field-value multipliers are shown in top right corners. (b) Plot of $\sqrt{2\pi r dr}|E(r)|$ for various initial ring radii R. The image of the initial Gaussian contribution is bound by $0 < r \lesssim w = 0.5$ mm (dashed line). The image of the initial ring contribution appears along the dash-dotted line. A strong phase-matched ring is seen in between.

and pump, respectively [10]. We solve Eq. (6) numerically, utilizing a fourth-order Runge-Kutta scheme.

After the crystal, the generated SH field is propagated to the output plane, neglecting again crystal-to-air power losses. Initial pump and resulting signal distributions at the output plane are shown in Fig. 3(a), considering $T = T_{pm}^0 = 114.5\,°C$ and $T = 113.6\,°C \neq T_{pm}^0$. For the FGB or FRB alone, the output plane signal observably inherits the initial structure (Gaussian or ring). However, for a superposition of the two, the signal shows a new component, corresponding to an STNPM scheme. This additional ring contains a larger part of the total power in the output plane for $T \neq T_{pm}^0$ relative to the $T = T_{pm}^0$ case. The reason is that here, while the collinear processes suffer from a thermally induced phase mismatch, the noncollinear scheme compensates for this mismatch.

We now study how this STNPM signal's ring power changes when T, W, and R are varied. The FGB from now on is fixed with $w = 0.5$ mm. Radial field distributions at the output plane for $T = 113.6\,°C$ ($\neq T_{pm}^0$) as a function R are obtained first. To account for the integrated intensity over a ring with radius r, the resultant field distribution (for each R) is multiplied by the factor $\sqrt{2\pi r dr}$, where r and dr are the radial coordinate and radial resolution of the output plane,

respectively. The resultant graph is shown in Fig. 3(b) for $1 \leqslant R \leqslant 8$ mm. Since the Gaussian component is fixed, its image is bound in the interval $0 < r \lesssim 0.5$ mm (white dashed line) in the output plane, regardless of the ring's radius. The distance between the input and output planes is about $2f$, so the input plane ring is imaged to $r \cong R$ (white dash-dotted line). Finally, between the individual locations of the original superposition components lies a strong contribution of the phase-matched central ring. The PM ring radius for an STNPM in this case ($T = 113.6\,°C$) is $R_{opt} \cong 4.9$ mm. The process is repeated to collect the values of PM radii R_{opt}, for various T. The result is shown in Fig. 8(b), along with the geometrical optics prediction by Eq. (3) (solid line). Precise values of small R_{opt} are harder to calculate from simulation, as all three components (Gaussian, ring and, central ring) overlap and make it difficult to isolate the central ring.

We now study the influence of the ring half-width W in two scenarios. First, we choose a temperature ($T = 113.6\,°C \neq T_{pm}^0$) and a corresponding PM radius ($R = R_{opt} = 4.9$ mm). By varying W we now obtain radial field distributions at the output plane [Fig. 4(a)]. As expected, all distribution maxima appear at the same $r \cong R_{opt}/2$. Larger W results in a reduced
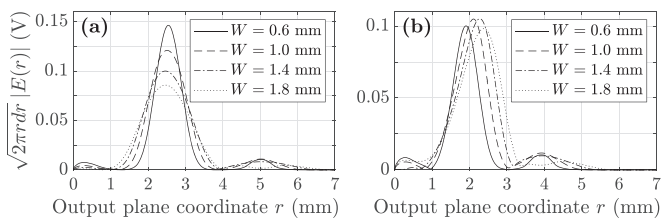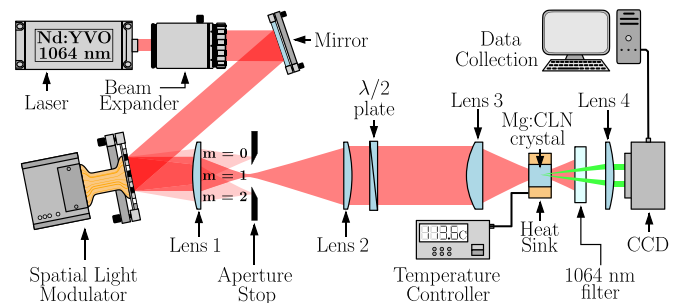

FIG. 4. Plot of $\sqrt{2\pi r dr}|E(r)|$ for (a) $R = 4.9$ mm and (b) $R = 3.9$ mm and various initial ring half-widths W. Here the crystal's temperature $T = 113.6\,°C$ corresponds to $R_{opt} = 4.9$ mm.

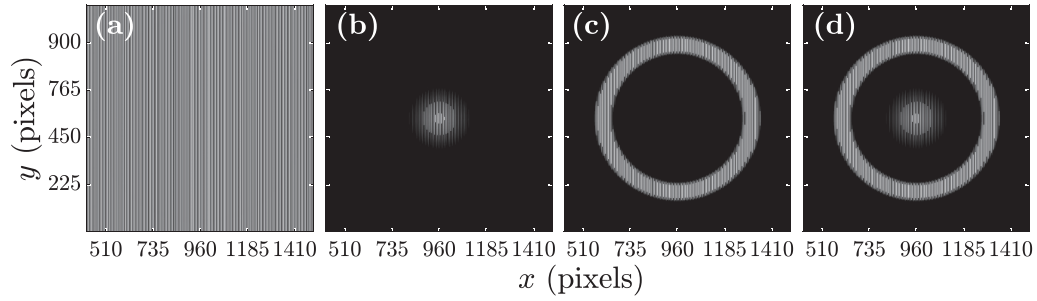FIG. 5. Experimental setup for STNPM in LiNbO$_3$.

FIG. 6. Initial SLM masks. (a) Only a first-order diffraction mask (grating) is applied, (b) a Gaussian-shaped beam generating mask is applied, (c) an annular ring-shaped beam generating mask is applied, and (d) superposition of (b) and (c) is applied.

peak field since the initial power is kept constant and wider initial rings reduce the initial peak field. Consequently, less power is transferred to the SH signal at the PM condition and the peak field in the output plane decreases. Additionally, the output plane central ring width is weakly increasing with W.

Second, we choose $R = 3.9$ mm $\neq R_{opt}$ (still $T = 113.6\,°$C) and again vary W. Figure 4(b) shows that now the peak field does not monotonically decrease as W increases; instead, for $W = 0.5$, 0.8 and 1.1 mm the field increases. The reason is that for $R = 3.9$ mm and $W > 1$ mm the ring contains the required $R_{opt} = 4.9$ mm and the PM condition can still be met. Nevertheless, increasing W further reduces the peak field again since the SH gain is not enough to compensate for the power reduction caused by the increasing input-plane ring's width. In addition, the central ring peak shifts as W increases, closer to the coordinate $r \cong R_{opt}/2$ corresponding to the PM radius R_{opt}.

IV. EXPERIMENTAL RESULTS

The experimental setup is shown in Fig. 5. A pulsed laser (InnoLas Picolo-AOT MoPa Nd:YVO) beam at $\lambda_0 = 1064$ nm central wavelength, repetition rate of 1 kHz, and pulse width of 800 ps is expanded to cover the area of the SLM. The SLM mask [11] contains a spatial diffraction grating component [Fig. 6(a)]. Only the first diffraction order is kept; all others are blocked by an aperture stop (after which the beam's power is $P \cong 1\,\mu$W). The beam is then focused into

the Mg:CLN crystal after passing through a $\lambda/2$ plate ensuring the correct beam polarization enters the crystal. We have used an Mg:CLN crystal grown by the Czochralski method [12], which has the appropriate refractive indices [13] and nonlinear coefficients [14,15]. The crystal (z cut with optic axis oriented perpendicular to the laser propagation) is located inside a custom-made copper heat sink, with temperature maintained by an external (ElectroTherm/Watlow PT100 S50) controller of resolution $0.1\,°$C. The pump beam is then blocked by a bandpass filter (Thor Labs FGB37), while the generated SH beam passes through it and is then imaged on the camera (Thor Labs DCC1240M, 1280×1024 pixels, 6.78×5.43 mm^2). Data from the camera are recorded and analyzed in MATLAB.

We use a Holoeye PLUTO-2.1 LCOS SLM to create and control the pump field, with an active area of 1920×1080 pixels (15.38×8.64 mm^2). Consequently, the maximal available ring radius is 540 pixels (4.32 mm). Lenses L1 and L2 serve as a magnifying $2\times$ telescope, doubling the maximal R available. The focusing lens L3 defines the angle θ. Values of R after L2 used are in the range of 50–440 pixels (800 μm to 7 mm) in steps of 5 pixels (80 μm). Temperatures used are in the range $113\,°$C $\lesssim T \lesssim 114.5\,°$C.

First we obtained noncritical PM at temperature $T_{pm}^0 = 114.5\,°$C of the crystal [4], by measuring the SH power with only the Gaussian mask applied on the SLM. This agrees with T_{pm}^0 of a similarly doped LiNbO$_3$ in the work of Schlarb and Betzler [16]. Then T is reduced to $113.6\,°$C
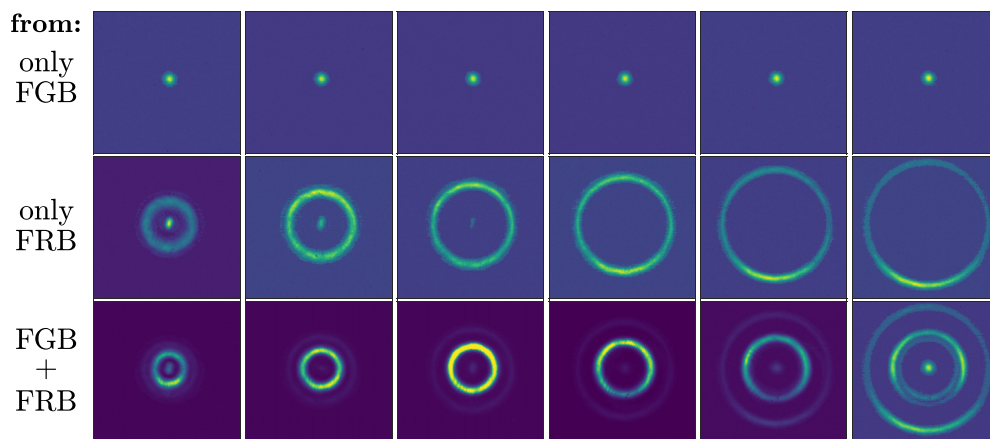

FIG. 7. Second-harmonic intensity (arbitrary units) on camera for a Gaussian (top row), annular ring (middle row), and both masks applied on the SLM (bottom). Columns differ by initial ring radii R (from left to right): 3.5, 4.1, 4.7, 5.3, 5.9, and 6.5 mm.
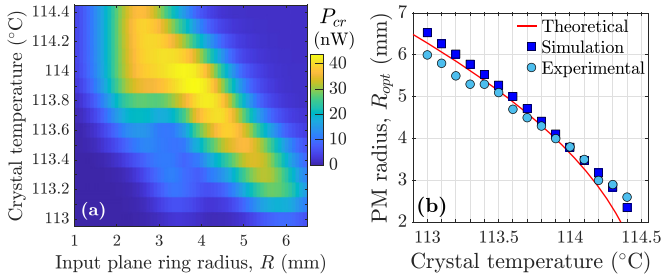
FIG. 8. (a) Measured SH central ring power for various initial ring radii and crystal temperatures. (b) Optimal ring radii vs crystal temperature (measurements, theoretical, and simulation predictions). The initial ring half-width in all cases is 1.8 mm.
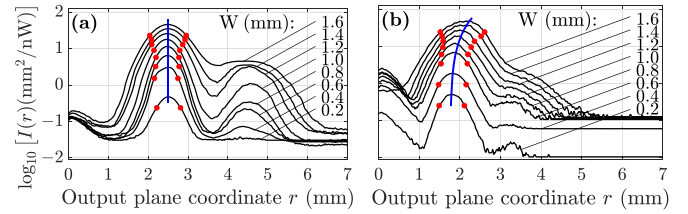

FIG. 9. Measured SH central ring radial intensity (in logarithmic scale) vs output plane coordinate for various half-widths W for (a) $R = R_{opt} = 4.9$ mm and (b) $R = 3.9$ mm $\neq R_{opt}$. The temperature in all cases is $T = 113.6\,°C$, corresponding to $R_{opt} = 4.9$ mm. Each horizontal pair of red dots indicates the FWHM of the SH central ring. Blue curves indicate the drift of the SH central ring's maximum towards $r \cong R_{opt}/2$.

to achieve $\Delta k_{cl} \neq 0$. Figure 7 shows the SH signal generated from each of the three initial SLM masks shown in Figs. 6(b)–(d), for various R values. The signal is not influenced by R for the Gaussian mask, as it is independent of it. It represents the case of collinear on-axis PM [Fig. 1(a)]. The middle row shows the SH generated by a ring mask and represents a collinear off-axis scheme [Fig. 1(b)]. The weak signal in the center of the images might be due to Raman-Nath-type diffraction employing the axial component of the pump wave vector. Finally, the bottom row shows the SH signal generated by the superposition, corresponding to the STNPM scheme [Fig. 1(c)]. The general behavior coincides with the simulation predictions [Fig. 3(a)]. Next we measured the power of the central ring as a function of R and T [Fig. 8(a)]. As expected, the PM radii increase for lower temperatures, to compensate for a growing Δk_{cl}. Figure 8(b) shows the PM radii R_{opt} as a function of T. The measurements indeed follow a square-root dependence of R_{opt} on T, predicted by approximation of Eq. (3) and simulation.

Finally, we measured the SH central ring intensity dependence on W (Fig. 9). Unlike that shown in Fig. 4(a), here the SH signal grows with increasing W, because the ratio $\beta = 2$ [see Eq. (4)] is controlled, but not the total light power covering the SLM. Wider rings then produce a stronger SH. As predicted by the simulation [Fig. 4(a)], wider rings do not shift the SH central ring maximum [Fig. 9(a)] for $R = R_{opt}$, only leading to a weak broadening of the SH central ring profile. In contrast, when $R \neq R_{opt}$ is chosen and W is increased [Fig. 9(b)], the SH central ring drifts towards a coordinate $r \cong R_{opt}/2$, corresponding to a PM radius of R_{opt} [Fig. 4(b)]. The ratio $\beta = 2$ was chosen in the experiment and in the simulation. This value was chosen quite arbitrarily, within a range that allows both the FGB and FRB components to be of

the same order of intensity inside the crystal. Otherwise, one of the components becomes dominant and SHG tends to be of the collinear type, either on-axis (Gaussian component is dominating) or off-axis (ring component is dominating).

V. CONCLUSION

We have shown theoretically and experimentally that PM can be achieved out of noncritical PM temperature using an additional optical spatial modulation of the pump beam. When both thermally induced and geometrical spatial mismatch are present they can compensate for each other. We showed that a noncollinear spatial modulation created by a superposition of Gaussian and annular ring beams inside a birefringent crystal can fulfill PM this way. As temperature decreases from its PM value, spatially tuned PM is achieved by introducing a more rapid spatial modulation, in terms of a larger initial ring radius.

An obvious advantage of our phase-matching scheme over other schemes of NCPM is that optical beam mode tuning is much faster than temperature tuning, which enables better stability of SHG in the face of environmental temperature fluctuations. The premise of controlling nonlinear optical processes with the optical mode structure of light can be further applied to various scenarios such as parametric down-conversion (in relation to quantum optics), to applications in nonlinear multimode fibers, and to computational optics.

[1] R. L. Sutherland, *Handbook of Nonlinear Optics* (CRC, Boca Raton, 2003).

[2] J. Lin, Non-linear crystals for tunable coherent sources, Opt. Quantum Electron. **22**, S283 (1990).

[3] R. W. Boyd, *Nonlinear Optics* (Academic, New York, 2020).

[4] See Supplemental Material at http://link.aps.org/supplemental/10.1103/PhysRevA.106.L031502 for geometric details of the setup and material properties of the MgO-doped LiNbO$_3$.

[5] T. Kong, H. Liu, X. Ge, D. Qu, S. Liu, S. Chen, L. Zhang, Y. Kong, R. Rupp, and J. Xu, Room temperature 90°

phase-matching in zirconium and magnesium co-doped lithium niobate crystals, Sci. Rep. **8**, 3865 (2018).

[6] A. Libster-Hershko, S. Trajtenberg-Mills, and A. Arie, Dynamic control of light beams in second harmonic generation, Opt. Lett. **40**, 1944 (2015).

[7] J. V. Thompson, B. H. Hokr, G. A. Throckmorton, D. Wang, M. O. Scully, and V. V. Yakovlev, Enhanced second harmonic generation efficiency via wavefront shaping, ACS Photon. **4**, 1790 (2017).

[8] L. Hareli, L. Lobachinsky, G. Shoulga, Y. Eliezer, L. Michaeli, and A. Bahabad, On-the-Fly Control of High-Harmonic Generation Using a Structured Pump Beam, Phys. Rev. Lett. **120**, 183902 (2018).

[9] S. Guha and L. P. Gonzalez, *Laser Beam Propagation in Nonlinear Optical Media* (CRC, Boca Raton, 2014), Vol. 1.

[10] J. R. Schwesyg, A. Markosyan, M. Falk, M. C. C. Kajiyama, D. H. Jundt, K. Buse, and M. M. Fejer, *Advances in Optical Materials, Istanbul, 2011* (Optica, Washington, DC, 2011), paper AIThE3.

[11] E. Bolduc, N. Bent, E. Santamato, E. Karimi, and R. W. Boyd, Exact solution to simultaneous intensity and phase encryption with a single phase-only hologram, Opt. Lett. **38**, 3546 (2013).

[12] J. Czochralski, Ein neues verfahren zur messung der kristallisationsgeschwindigkeit der metalle, Z. Phys. Chem. **92U**, 219 (1918).

[13] Y. Furukawa, K. Kitamura, A. Alexandrovski, R. Route, M. Fejer, and G. Foulon, Green-induced infrared absorption in MgO doped LiNbO$_3$, Appl. Phys. Lett. **78**, 1970 (2001).

[14] R. Klein, G. Kugel, A. Maillard, K. Polgár, and A. Péter, Absolute non-linear optical coefficients of LiNbO$_3$ for near stoichiometric crystal compositions, Opt. Mater. **22**, 171 (2003).

[15] I. Shoji, T. Kondo, A. Kitamoto, M. Shirane, and R. Ito, Absolute scale of second-order nonlinear-optical coefficients, J. Opt. Soc. Am. B **14**, 2268 (1997).

[16] U. Schlarb and K. Betzler, Influence of the defect structure on the refractive indices of undoped and Mg-doped lithium niobate, Phys. Rev. B **50**, 751 (1994).